NL-InSAR: Non-Local Interferogram Estimation

Charles-Alban Deledalle, *Student Member, IEEE,* Loïc Denis and Florence Tupin, *Senior Member, IEEE*

Abstract—Interferometric synthetic aperture radar (InSAR) data provides reflectivity, interferometric phase and coherence images, which are paramount to scene interpretation or low-level processing tasks such as segmentation and 3D reconstruction. These images are estimated in practice from hermitian product on local windows. These windows lead to biases and resolution losses due to local heterogeneity caused by edges and textures. This paper proposes a non-local approach for the joint estimation of the reflectivity, the interferometric phase and the coherence images from an interferometric pair of co-registered single-look complex (SLC) SAR images. Non-local techniques are known to efficiently reduce noise while preserving structures by performing a weighted averaging of similar pixels. Two pixels are considered similar if the surrounding image patches are "resembling". Patch-similarity is usually defined as the Euclidean distance between the vectors of graylevels. In this paper a statistically grounded patch-similarity criterion suitable to SLC images is derived. A weighted maximum likelihood estimation of the SAR interferogram is then computed with weights derived in a data-driven way. Weights are defined from intensity and interferometric phase, and are iteratively refined based both on the similarity between noisy patches and on the similarity of patches from the previous estimate. The efficiency of this new interferogram construction technique is illustrated both qualitatively and quantitatively on synthetic and true data.

Index Terms—Estimation, Non-local means, Interferometric Synthetic Aperture Radar (InSAR)

I. INTRODUCTION

INTERFEROMETRIC synthetic aperture radar (InSAR) aims to recover information about heights or displacements in a scene. Two SAR complex images are sensed by two parallel-passes separated by a spatial baseline. The amplitude components provide information on the reflectivity, and, after co-registration of the two images, the phase difference is directly related to the path delay between the two waves. This phase difference, denoted as interferometric phase, can be used to recover the height or the movement [1]. Interferences of elementary scatterers causes speckle effects on the measured amplitudes of the backscattered waves. Due to temporal and spatial variations between the two acquisitions, the speckle components between the two acquisitions (i.e. the underlying scattering processes) present a small decorrelation which affects the interferometric phase [2]. The coherence between

the two acquisitions appears then as a crucial indicator of the reliability of the interferometric phase. This paper focuses on the joint estimation of the three InSAR parameters: the reflectivity of the scene, the interferometric phase and the coherence. Note that the orbital component (flat earth and orbital inaccuracies) of the interferometric phase is assumed to have been previously removed from the phase images to ensure the phase stationarity in homogeneous areas.

An interferometric pair of co-registered single-look complex (SLC) SAR images can be modeled on each pixel with a joint parametric distribution grounded on three physical parameters: the reflectivities, the actual interferometric phase and the coherence. Let z and z' be the complex values of two corresponding pixels in the two SLC images. According to Goodman's model [3], z and z' follow a zero-mean complex circular Gaussian distribution:

$$p(z, z'|\Sigma) = \frac{1}{\pi^2 det(\Sigma)} \exp\left[-\left(z^* z'^*\right)\Sigma^{-1}\begin{pmatrix} z \\ z' \end{pmatrix}\right] \quad (1)$$

with Σ a 2×2 covariance matrix, which can be decomposed as follows:

$$\begin{aligned}\Sigma &= \mathbb{E}\left\{\begin{pmatrix} z \\ z' \end{pmatrix}\left(z^* z'^*\right)\right\} \\ &= \begin{pmatrix} R & \sqrt{RR'}De^{j\beta} \\ \sqrt{RR'}De^{-j\beta} & R' \end{pmatrix}\end{aligned} \quad (2)$$

where R and R' are the underlying reflectivities, β the actual interferometric phase, D the coherence between the two acquisitions and $\mathbb{E}$ denotes the mathematical expectation. Note that we use the term reflectivity but R is actually a quantity linked to the backscattering coefficient and thus to the radar cross section per unit volume [4].

Numerous estimators have been proposed to estimate the covariance matrix Σ. The majority have been specially designed to estimate only one of the three parameters:

- Amplitude denoising is usually achieved by using spatially adaptive filtering based on local statistics in order to cope with the signal-dependent multiplicative speckle noise [5]–[9]. We refer the reader to the survey of R. Touzi [10] for a deeper analysis of such methods. The most recent approaches use parametric distributions based wavelet soft-thresholding, with spatially adaptive filtering in the wavelet domain [11], [12], or with logarithmically transformed amplitude [13]–[15]. Non-local estimation of the reflectivity has also been proposed in [16], [17].
- Interferometric phase restoration is usually expressed as a problem of phase denoising and phase unwrapping. This paper focuses only on the first problem namely

the estimation of the noise-free wrapped interferometric phase. Recent techniques achieve this goal by finding the best local polynomial approximation in an adaptive window [18]–[20].

- The coherence is an indicator of the reliability of the phase quality but is also widely used to detect temporal changes in remote sensing applications. The main problem in the coherence estimation is the introduction of a bias towards higher values due to the limited number of averaged samples. Different methods have been proposed to improve the quality of the estimation in terms of bias and variance [21], [22]. A recent approach, proposed by López Martínez *et al.*, is based on wavelet transform [23].

Other estimators take advantage of Goodman's model to provide a joint estimation of the three parameters. The majority of them are based on local statistics, and therefore affect the spatial resolution while few estimators achieve this goal without significant loss of resolution:

- The usual parameter estimation approach is the direct application of the spatial stationarity principle. It considers noisy samples in a window centered on a given pixel as all following the distribution of that pixel. This leads to the boxcar filter which locally estimates the complex covariance matrix Σ over a sliding window. Known as complex multi-looking, this operation is widely used in practice to provide an estimate of the reflectivity, the actual interferometric phase and the coherence. The fundamental limitation of this technique comes from the loss of resolution on the estimated images, since the same smoothing effect is equally applied to homogeneous regions, and to edges or textured zones. Moreover, as mentioned above, the coherence estimate is biased and finally overestimated due to the limited number of samples in the local window.

- In [24], [25], Lee *et al.* proposed to use adaptive filtering for polarimetric and interferometric SAR denoising. Instead of estimating the parameters over a rectangular sliding window, a directional window is locally selected among eight edge-aligned windows, according to the local gradient of the amplitude images. A complex covariance matrix is estimated over the obtained window which is used in the linear minimum mean square error estimator to obtain the denoised covariance matrix Σ. This preserves edge structures, since values of pixels on each side of the edge are never combined together, avoiding then smoothing effects. Unfortunately, this method tends to leave a high variance in homogeneous area and create some undesired artifacts.

- Intensity-driven adaptive-neighborhood (IDAN) technique has been proposed in [26] for polarimetric and interferometric SAR parameter estimation. Following the idea of filtering over directional windows, IDAN performs a complex multi-looking operation on an adaptive neighborhood. This adaptive neighborhood is constructed with a region growing algorithm where the most similar adjacent pixels are selected iteratively according to their intensity values. The adaptive neighborhood aims to se-

lect as many pixels as possible, all following the same statistical population as the considered pixel. This decreases the resolution loss in the estimation since noisy values coming from other populations are rejected. Due to its window-shape adaptivity, IDAN achieves the best trade-off between residual noise and resolution loss among window-based methods. However, due to its connectivity constraint, IDAN leaves a high variance in regions where there are only few adjacent similar pixels.

Rather than restricting the similar pixels to belong to a local neighborhood such as rectangular windows, directional windows or spatially connected components, we choose to also consider pixels that are far apart. Indeed, SAR images have usually high resolutions compared to the scale of the topography and deformation effects, then most of the patterns can occur several times. Our idea, based on the non-local means filter (NL means) [27], is to exploit these redundant patterns to select a large set of pixels to combine for the estimation of each given pixel. A pixel is assumed to come from the same statistical population as the given pixel if the patches that surround the two pixels are similar. This patch-based estimator can be considered as *non-local* since pixel values somewhat far apart can be averaged together, depending on the surrounding patch-similarity. The non-local interferometric SAR (NL-InSAR) estimator is based on the patch-based estimator introduced in [17] for image denoising. Instead of combining pixels from a binary set, a membership value is computed according to a patch-based similarity criterion. This membership value is then used in a weighted maximum likelihood estimator to produce the desired parameters. Unlike directional windows based filtering and IDAN which use only the intensity to select the suitable samples, NL-InSAR uses a probabilistic criterion based on both the intensities and the interferometric phases that surround two given patches (it is assumed that the orbital component has been previously removed from the phase images). Moreover, the estimation is refined iteratively by including the similarity between pre-estimated patches of the InSAR parameters. This iterative process noticeably improves the estimation performances.

II. NON-LOCAL InSAR ESTIMATION

A. *Weighted maximum likelihood estimation*

This section presents the method proposed for NL-InSAR to estimate the three parameters R, β and D. It seems reasonable to consider equal the (true) reflectivities of each pair of corresponding pixels, i.e $R = R'$ in (2). This hypothesis is naturally verified in regions with good coherence. By reducing the number of degrees of freedom (from 4 to 3 unknowns), the estimation variance is improved. Denoising techniques must trade-off variance reduction and resolution preservation. As the sample size is restricted by resolution preservation considerations, it is desirable to reduce the variance with such a hypothesis. Let $A = |z|$ and $A' = |z'|$ be the amplitudes and $\phi = \arg(zz'^*)$ the noisy interferometric phase which is compensated for the flat earth phase. From (1) and (2), with the constraint $R = R'$, the InSAR observations are related to

the InSAR parameters R, D and β by [28]:

$$p(A, A', \phi | R, D, \beta) = \frac{2AA'}{\pi R^2 (1 - D^2)} \times$$
$$\exp\left(-\frac{A^2 + A'^2 - 2DAA' \cos(\phi - \beta)}{R(1 - D^2)}\right). \quad (3)$$

NL-InSAR uses the weighted maximum likelihood estimator (WMLE) which can be interpreted as an extension of the weighted average performed in the NL means [17]. Formally, the WMLE defines at each site s the estimate $\hat{\Theta}_s = (\hat{R}_s, \hat{\beta}_s, \hat{D}_s)$ as:

$$\hat{\Theta}_s = \arg\max_{\Theta} \sum_t w(s, t) \log p(\mathcal{O}_t | \Theta) \quad (4)$$

where $\mathcal{O}_t = (A_t, A'_t, \phi_t)$ is the observation at site t and $w(s, t) > 0$ is a data-driven weight. WMLE is known to reduce the mean squared error by reducing the variance of the estimate at the cost of a bias introduced by samples that follow a distribution with parameters Θ_t different to Θ_s [29]. The WMLE framework has already been applied successfully to image denoising in [30] and to non-local estimation in [17]. For InSAR data, the maximum likelihood estimator of the covariance matrix Σ is well-known to be the sample estimate of the covariance matrix. The parameters R, R', β and D are then given by term identification which leads to compute the sample estimate of the complex cross-correlation. Seymour and Cumming in [31] derived the maximum likelihood estimator of (3) which differs from the classical sample estimate since it assumes that $R = R'$. From their work, we extend their formulation to the case of WMLE, which is given, for $\Theta_s = (R_s, \beta_s, D_s)$ and $\mathcal{O}_t = (A_t, A'_t, \phi_t)$, by:

$$\left.\begin{array}{rcl} \hat{R}_s &=& \dfrac{a}{N}, \\ \hat{\beta}_s &=& -\arg x, \\ \hat{D}_s &=& \dfrac{|x|}{a} \end{array}\right\} \quad (5)$$

$$\left.\begin{array}{rcl} \text{with} \quad a &=& \displaystyle\sum_t w(s, t) \dfrac{|z_t|^2 + |z'_t|^2}{2}, \\ x &=& \displaystyle\sum_t w(s, t)\, z_t z_t'^{*}, \\ N &=& \displaystyle\sum_t w(s, t). \end{array}\right\} \quad (6)$$

Equation (5) defines the same estimator of reflectivity and phase as the sample estimator. The coherence estimator differs in the denominator: a in equation (5), and $\sqrt{\sum_t w(s, t) |z_t|^2 |z'_t|^2}$ in the sample estimate. When the assumption $R = R'$ holds, it is shown in [31] that their estimator of the coherence (and thus that defined in (5)) is more efficient than the classical sample estimate. For instance, an estimate of the coherence can be obtained without averaging in a local neighbourhood whereas the sample estimator requires to average at least two pixels to define a coherence.

In [17], we take inspiration of the non-local means algorithm to define the weights $w(s, t)$. The two observations $\mathcal{O}_s$ and $\mathcal{O}_t$ are considered to come from the same statistical population, i.e $\Theta_s = \Theta_t$, provided that the patches Δ_s and Δ_t that surround the two pixels s and t are similar. Figure 1 illustrates the procedure. At each site s, the pixels t are inspected sequentially
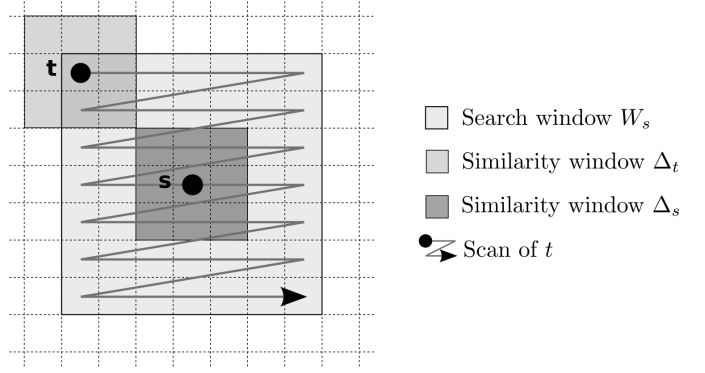

Fig. 1. WMLE combines for each site s the information of pixels t according to the similarity between two patches Δ_s and Δ_t centered respectively around the sites s and t.

to produce a weight by comparing the two noisy patches Δ_s and Δ_t. Once all weights $w(s, t)$ are computed, the WMLE is obtained according to (4). Note that for complexity reasons, the pixels t are restricted to a large window W_s centered around the site s. In the non-local means the similarity between the two patches Δ_s and Δ_t is given by an Euclidean distance of the intensity values. On InSAR data, such a distance cannot be used directly since it does not consider the statistical nature of the multi-dimensional observations. In [17], we showed that the Euclidean distance can be substituted by a similarity criterion grounded on statistical considerations for non-additive or non-Gaussian noises. The same approach can be applied here for InSAR data.

B. Similarity between noisy patches

We define patch similarity as a measure of how likely the two patches $\mathcal{O}_{\Delta_s}$ and $\mathcal{O}_{\Delta_p}$ could be considered as two noisy realizations of the same noiseless patch Θ_Δ. Given the independence assumption (i.e. noise is considered uncorrelated), patch similarity can be computed pixelwise. The weight $w(s, t)$ is then set as a function of the likelihood [17]:

$$w(s, t) \triangleq p(\mathcal{O}_{\Delta_s}, \mathcal{O}_{\Delta_t} | \Theta_{\Delta_s} = \Theta_{\Delta_p} = \Theta_\Delta)^{1/h} \quad (7)$$
$$= \prod_k p(\mathcal{O}_{s,k}, \mathcal{O}_{t,k} | \Theta_{s,k} = \Theta_{t,k})^{1/h} \quad (8)$$

where h is a filtering parameter (a larger h leads to less discriminative weights), and s,k and t,k denote the k-th pixel in each patch Δ_s and Δ_t. For reason of readability, the pixels s,k and t,k will be denoted respectively by 1 and 2 in the following.

As the "true" values Θ are unknown, the similarity likelihood $p(\mathcal{O}_1, \mathcal{O}_2 | \Theta_1 = \Theta_2)$ is computed by considering all possible values for Θ (under a uniform prior):

$$\int p(\mathcal{O}_1 | \Theta_1 = \Theta) p(\mathcal{O}_2 | \Theta_2 = \Theta) \mathrm{d}\Theta. \quad (9)$$

Unfortunately, (9) is not necessarily scale-invariant which is not satisfying to model the weights in the WMLE. However, its definition depends on the chosen observation space of $\mathcal{O}$. The choice of $\mathcal{O}$ affects the similarity likelihood by a multiplicative factor (namely the Jacobian). Then, the search of
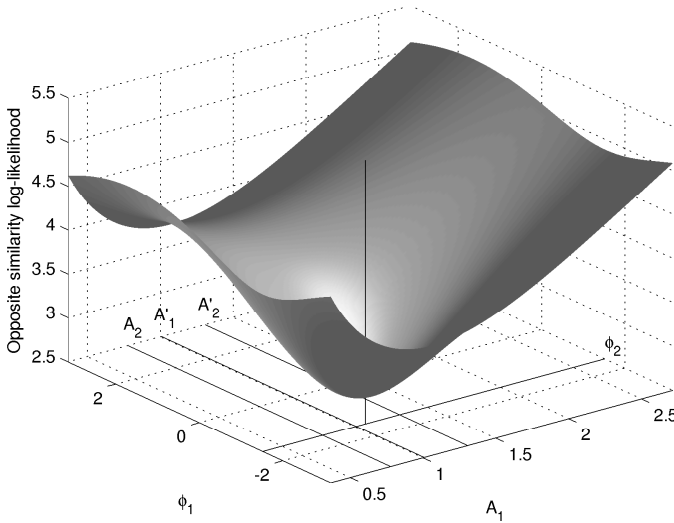
Fig. 2. Similarity log-likelihood with respect to A_1 and ϕ_1 for the given values A'_1, A_2, A'_2 and ϕ_2.

a suitable observation space can lead to obtain a scale-invariant similarity likelihood. Given the probability density function of the original observation $\mathcal{O}$ and Φ a mapping function from the original observation space to the suitable observation space, the similarity likelihood can be defined as:

$$p(\mathcal{O}_1, \mathcal{O}_2 | \Theta_1 = \Theta_2) = \left| \frac{d\Phi}{d\mathcal{O}_1}(\mathcal{O}_1) \right|^{-1} \left| \frac{d\Phi}{d\mathcal{O}_2}(\mathcal{O}_2) \right|^{-1}$$
$$\times \int p(\mathcal{O}_1 | \Theta_1 = \Theta) p(\mathcal{O}_2 | \Theta_2 = \Theta) \mathrm{d}\Theta. \qquad (10)$$

In case of InSAR data, a simple dimensional analysis shows that choosing $\Phi : (A, A', \phi) \mapsto (\sqrt{A}, \sqrt{A'}, \phi)$ gives a scale-invariant similarity criterion. According to this, equation (10) and appendix A, the similarity likelihood, for $\mathcal{O}_k = (A_k, A'_k, \phi_k)$, $k = 1..2$, is given by:

$$p(\mathcal{O}_1, \mathcal{O}_2 | \Theta_1 = \Theta_2) =$$
$$\sqrt{\frac{\mathcal{C}^3}{\mathcal{B}}} \left(\frac{\mathcal{A} + \mathcal{B}}{\mathcal{A}} \sqrt{\frac{\mathcal{B}}{\mathcal{A} - \mathcal{B}}} - \arcsin \sqrt{\frac{\mathcal{B}}{\mathcal{A}}} \right) \qquad (11)$$

with
$$\mathcal{A} = (A_1^2 + A_1'^2 + A_2^2 + A_2'^2)^2,$$
$$\mathcal{B} = 4(A_1^2 A_1'^2 + A_2^2 A_2'^2 + 2A_1 A_1' A_2 A_2' \cos(\phi_1 - \phi_2)),$$
$$\mathcal{C} = A_1 A_1' A_2 A_2'.$$

Figure 2 represents the similarity likelihood defined in (11) with respect to the values of A_1 and ϕ_1 for given values of A'_1, A_2, A'_2 and ϕ_2. To emphasize the variations of the similarity likelihood, the negative logarithm of the similarity likelihood $-\log f(\mathcal{O}_1, \mathcal{O}_2 | \Theta_1 = \Theta_2)$ is plotted. The criterion is minimum when observed data are identical: $A_1 = A_2$, $A'_1 = A'_2$ and $\phi_1 = \phi_2$. Moreover, this criterion manages well with the phase wrapping, without creating discontinuities when ϕ_1 jumps from $-\pi$ to π due to wrapping. For a given value of A_1, the criterion is minimum when ϕ_1 and ϕ_2 are in-phase and maximum when they are out-of-phase. An interesting property of the similarity likelihood is that for a given pair of observed phases ϕ_1 and ϕ_2, the criterion is more discriminant when the
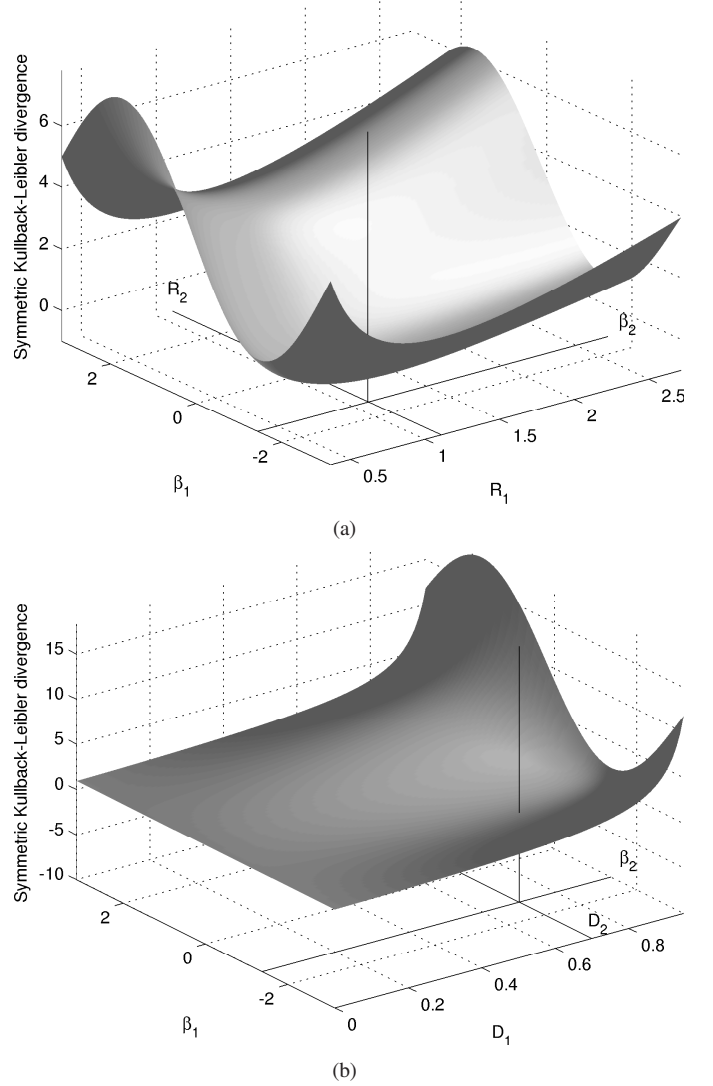

(a)

(b)

Fig. 3. Symmetric Kullback-Leibler divergence with respect to (a) $\hat{R}_1$ and $\hat{\beta}_1$ for the given values of $\hat{R}_2$, $\hat{\beta}_2$ with $\hat{D}_1 = \hat{D}_2 = 0.7$, and (b) $\hat{D}_1$ and $\hat{\beta}_1$ for the given values of $\hat{\beta}_2$, $\hat{D}_2$ with $\hat{R}_1 = \hat{R}_2$.

observed amplitudes are closer, and is less discriminant when the amplitudes differ.

C. Similarity between pre-estimated patches

In [17], it has been proposed to refine the weights iteratively by using at iteration i the previously estimated parameters $\hat{\Theta}^{i-1}$. Instead of approaching the similarity likelihood, we try to approach the *a posteriori* probability defined by the Bayes relation:

$$p(\Theta_1 = \Theta_2 | \mathcal{O}) \propto \underbrace{p(\mathcal{O}_1, \mathcal{O}_2 | \Theta_1 = \Theta_2)}_{\text{likelihood term}} \times \underbrace{p(\Theta_1 = \Theta_2)}_{\textit{prior term}} \quad (12)$$

The idea is to use the pre-estimated image $\hat{\Theta}^{i-1}$ to measure the validity of the hypothesis $\Theta_1 = \Theta_2$. The equality $\Theta_1 = \Theta_2$ is assumed to be more likely to hold as the data distributions with parameters $\hat{\Theta}_1^{i-1}$ and $\hat{\Theta}_2^{i-1}$ get closer. Polzehl and Spokoiny showed that the Kullback-Leibler divergence between these two data distributions provides a statistic test of the hypothesis $\Theta_1 = \Theta_2$ [30]. The *prior* term is defined by a symmetrical

version of the Kullback-Leibler divergence over an exponential decay function:

$$p(\Theta_1 = \Theta_2) \propto \exp\left[-\frac{1}{T}SD_{KL}(\hat{\Theta}_1^{i-1}, \hat{\Theta}_2^{i-1})\right]$$

where $SD_{KL}(\hat{\Theta}_1^{i-1}, \hat{\Theta}_2^{i-1}) =$

$$\int \left(p(\mathcal{O}|\hat{\Theta}_1^{i-1}) - p(\mathcal{O}|\hat{\Theta}_2^{i-1})\right) \log \frac{p(\mathcal{O}|\hat{\Theta}_1^{i-1})}{p(\mathcal{O}|\hat{\Theta}_2^{i-1})} \, d\mathcal{O} \quad (13)$$

and $T > 0$ is a positive real value. The parameters T and h act as dual parameters to balance the trade-off between the noise reduction and the fidelity of the estimate [30]. According to appendix B, the symmetrical Kullback-Leibler divergence in (13), for $\hat{\Theta}_k = \left(\hat{R}_k, \hat{\beta}_k, \hat{D}_k\right)$, $k = 1..2$, is given by:

$$SD_{KL}(\hat{\Theta}_1, \hat{\Theta}_2) = \frac{4}{\pi}\left[\frac{\hat{R}_1}{\hat{R}_2}\left(\frac{1 - \hat{D}_1\hat{D}_2\cos(\hat{\beta}_1 - \hat{\beta}_2)}{1 - \hat{D}_2^2}\right) + \frac{\hat{R}_2}{\hat{R}_1}\left(\frac{1 - \hat{D}_1\hat{D}_2\cos(\hat{\beta}_1 - \hat{\beta}_2)}{1 - \hat{D}_1^2}\right) - 2\right].$$

(14)

Figure 3 represents the symmetric Kullback-Leibler divergence defined in (14). In 3.a, the variations are given with respect to the values of $\hat{R}_1$ and $\hat{\beta}_1$, for given values of $\hat{R}_2$ and $\hat{\beta}_2$ with $\hat{D}_1 = \hat{D}_2 = 0.7$. In 3.b, the variations are given with respect to the values of $\hat{\beta}_1$ and $\hat{D}_1$, for given values of $\hat{\beta}_2$ and $\hat{D}_2$ with $\hat{R}_1 = \hat{R}_2$. The criterion decreases when all parameters at pixel $_1$ get closer to the parameters at pixel $_2$ and becomes null when the parameters are equal. Moreover, this criterion manages well with the phase wrapping, without creating discontinuities when $\hat{\beta}_1$ moves from $-\pi$ to π. For a given value of $\hat{R}_1$, the criterion is minimum when $\hat{\beta}_1$ and $\hat{\beta}_2$ are in-phase and maximum when they are out-of-phase. Note the satisfying behavior of the similarity criterion: the better the coherence (i.e., closer to 1), the larger the phase similarity, since phases are then more reliable.

D. Enforcing a minimum amount of smoothing

It is desirable to enforce a minimum amount of smoothing (i.e. variance reduction) in the denoising technique. In an image, some patches are (almost) unique (i.e. not found elsewhere inside the search window). The direct application of the algorithm would produce highly noisy estimates for the central value of these patches since the weighted maximum likelihood estimation would be computed over too few samples. In [17] this was not an issue for amplitude denoising. When considering iterative joint amplitude-phase-coherence estimation, the high variance of the estimator for "rare" patches leads to a decrease of the similarity between pre-estimated patches with the iterations. At the algorithm end, the resulting denoised images contain regions of high residual variance.

To guarantee a minimum amount of smoothing, and therefore limit the variance of the estimation, we propose to estimate the equivalent number of looks of the denoised pixels. Due to our non-local (data driven) approach, the equivalent number of looks varies from one pixel to another. It depends on the number of similar patches found in the search window, and can be approximated, for each pixel s, by:

$$\hat{L}_s = \frac{\left(\sum_t w(s,t)\right)^2}{\sum_t w(s,t)^2} \quad (15)$$

according to the variance reduction of a weighted average for the reflectivity and [20] for the interferometric phase. To enforce a minimum amount of smoothing, we suggest to redefine the weights $w(s,t)$ in the cases where the equivalent number of looks $\hat{L}_s$ falls below a given threshold L_{min}. An option is to redistribute equally the weights of the L_{min} most similar patches whenever $\hat{L}_s < L_{min}$. "Rare" patches often contain a bright scatterer. To prevent from biasing the estimation, we propose to restrict the selection of the L_{min} patches to those whose central value is not too bright compared to that of the reference patch, following the ideas of [32]–[34]. The correction of the weights can be performed as follows:

- Compute $\hat{L}_s$ for each pixel s,
- If $\hat{L}_s < L_{min}$, redistribute the L_{min} highest weights:
  - Create a vector $\mathbf{w}$ containing all the weights $w(s,t)$ such that $A_t < 2A_s$,
  - Sort the vector $\mathbf{w}$ in descending order,
  - Redistribute equally the weights of the L_{min} most similar pixels:

$$\mathbf{w}_k \leftarrow \frac{1}{L_{min}} \sum_{l=1}^{L_{min}} \mathbf{w}_l \quad \forall k \in 1..L_{min} \quad (16)$$

III. ALGORITHM

This section describes the whole procedure used in NL-InSAR. At each site s, the pixels t present in the search window W_s are inspected sequentially to produce a weight by comparing two surrounding patches Δ_s and Δ_t. For each corresponding pixels $_{s,k}$ and $_{t,k}$ in Δ_s and Δ_t, the similarity is computed by comparing noisy observations $\mathcal{O}_{s,k}$ and $\mathcal{O}_{t,k}$ (11) and the pre-estimated parameters $\hat{\Theta}_{s,k}^{i-1}$ and $\hat{\Theta}_{t,k}^{i-1}$ (14). These similarities are aggregated to produce the weights $w(s,t)$. In practice, the logarithm of the weights is computed to limit numerical errors. The weight $w(s,t)$ is then used to increment the accumulators a, x and N (6). Once all weights are obtained for each site t, the minimum noise reduction procedure is performed (Section II-D) before computing the parameters $\hat{\Theta}_s^i$ (5). The procedure is performed iteratively. Indeed, at the end of the iteration $i - 1$, the estimated parameters provide the pre-estimated parameters $\hat{\Theta}^{i-1}$ used at iteration i. The procedure is repeated until there is no more change between two consecutive estimates. In practice, the first pre-estimates can be chosen as constant parameter images, i.e. with constant reflectivity, phase and coherence. According to (12), (13) and (14), this is equivalent to performing the first iteration of NL-InSAR with weights based only on the likelihood term. Finally, at least ten iterations have to be performed to reach the best estimate.

The pseudo-code of NL-InSAR is given in Figure 4. The algorithm complexity is $O(|\Omega||W||\Delta|)$ where $|\Omega|$, $|W|$ and $|\Delta|$ are respectively the image size, the search window size and the similarity patch-size. Several optimizations of the

---

Algorithm Non Local InSAR (NL-InSAR)

Input: $\mathcal{O} = (A, A', \phi)$ and $\hat{\Theta}^{i-1} = \left(\hat{R}^{i-1}, \hat{\beta}^{i-1}, \hat{D}^{i-1} \right)$

Output: $\hat{\Theta}^i = \left(\hat{R}^i, \hat{\beta}^i, \hat{D}^i \right)$

for all pixels s of the image **do**

    Initialize the accumulators a, x and N to zero

    for all pixels t in W_s **do**

        $\log w(s,t) \leftarrow 0$

        for all pixels s, k and t, k in Δ_s and Δ_t **do**

            Compute $f(\mathcal{O}_{s,k}, \mathcal{O}_{t,k} \mid \Theta_{s,k} = \Theta_{t,k})$

                              $\triangleright$ use eq. (11)

            Compute $SD_{KL}(\hat{\Theta}^{i-1}_{s,k}, \hat{\Theta}^{i-1}_{t,k})$ $\triangleright$ use eq. (14)

            $\log w(s,t) \leftarrow \log w(s,t)$

                $+\frac{1}{h} \log f(\mathcal{O}_{s,k}, \mathcal{O}_{t,k} \mid \Theta_{s,k} = \Theta_{t,k})$

                $-\frac{1}{T} SD_{KL}(\hat{\Theta}^{i-1}_{s,k}, \hat{\Theta}^{i-1}_{t,k})$

        end for

        Increment the accumulators a, x and N

                                $\triangleright$ use eq. (6)

    end for

    Insure a minimum noise reduction $\triangleright$ see sec. II-D

    Compute $\hat{R}^i_s, \hat{\beta}^i_s$ and $\hat{D}^i_s$ $\triangleright$ use eq. (5)

end for

return $\left(\hat{R}^i, \hat{\beta}^i, \hat{D}^i \right)$

Fig. 4. Pseudo-code of the non local InSAR algorithm. The procedure has to be repeated iteratively. At iteration i the pre-estimated parameters $\hat{R}^{i-1}$, $\hat{\beta}^{i-1}$, $\hat{D}^{i-1}$ are used to refine the estimates. In practice, the first pre-estimates can be chosen as constant parameter images, and at least ten iterations have to be performed to reach the best estimate.

non-local means have been proposed in [35]–[37]. We have extended the solution proposed by Darbon *et al.* in [38] for the NL-InSAR algorithm with a time complexity given by $O(4|\Omega||W|)$. Finally, the computation time of our method is of about 160 seconds per iteration for an image of size $|\Omega| = 512 \times 512$ and windows of size $|W| = 21 \times 21$ and $|\Delta| = 7 \times 7$ using an Intel Pentium D 32-bit, 3.20GHz.

IV. EXPERIMENTS AND RESULTS

This section presents quantitative and qualitative results of the proposed estimator. For reasons of space and visibility, only small images are shown here. To assess the quality of the denoising methods, the reader can compare the full size images at http://www.perso.telecom-paristech.fr/~deledall/nlinsar.php. Some complementary comparisons are provided on this web-page.

A. Results on synthetic data

This section presents qualitative and numerical results obtained on simulated InSAR data. Given the true images of reflectivity R, interferometric phase β and coherence D, two single-look complex (SLC) images z_1 and z_2 are generated according to the model presented in section I. The simulation procedure, similar to that for simulating a polarimetric InSAR image [24], is as follows:
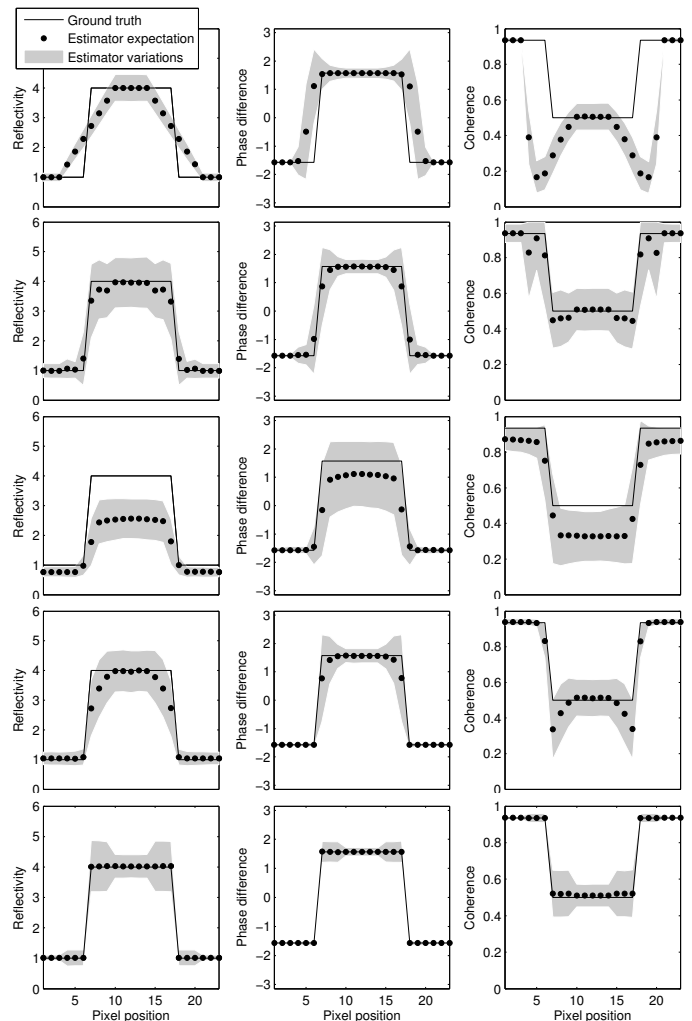

Fig. 5. Statistical answer on a rectangular function obtained from top to bottom by the boxcar estimator, Lee's estimator, the IDAN estimator, the non-iterative NL-InSAR estimator and the (iterative) NL-InSAR estimator.

- Compute a matrix L such that $\Sigma = LL^*$. For example, the lower triangle matrix L in the Cholesky decomposition is a good candidate:

$$ L = \sqrt{R} \begin{pmatrix} 1 & 0 \\ De^{-j\beta} & \sqrt{1-D^2} \end{pmatrix}, \qquad (17) $$

- Generate two independent complex random variables x_1, x_2 according to (1) with an identity covariance matrix,
- Finally, the correlated complex random variables z_1, z_2 are given by:

$$ \begin{pmatrix} z_1 \\ z_2 \end{pmatrix} = L \begin{pmatrix} x_1 \\ x_2 \end{pmatrix}. \qquad (18) $$

Once the two SLC SAR images are generated, the three InSAR parameters are estimated and compared to the known actual parameters. Our NL-InSAR estimator is applied with a search window of size $|W| = 21 \times 21$ and a similarity window of size $|\Delta| = 7 \times 7$. The parameters h and T are set as described in [17] which leads to the values $h = 12$ and $T = 0.2|\Delta|$. A minimum noise reduction of level $L_{min} = 10$ is maintained. We use 10 iterations of the iterative NL-InSAR
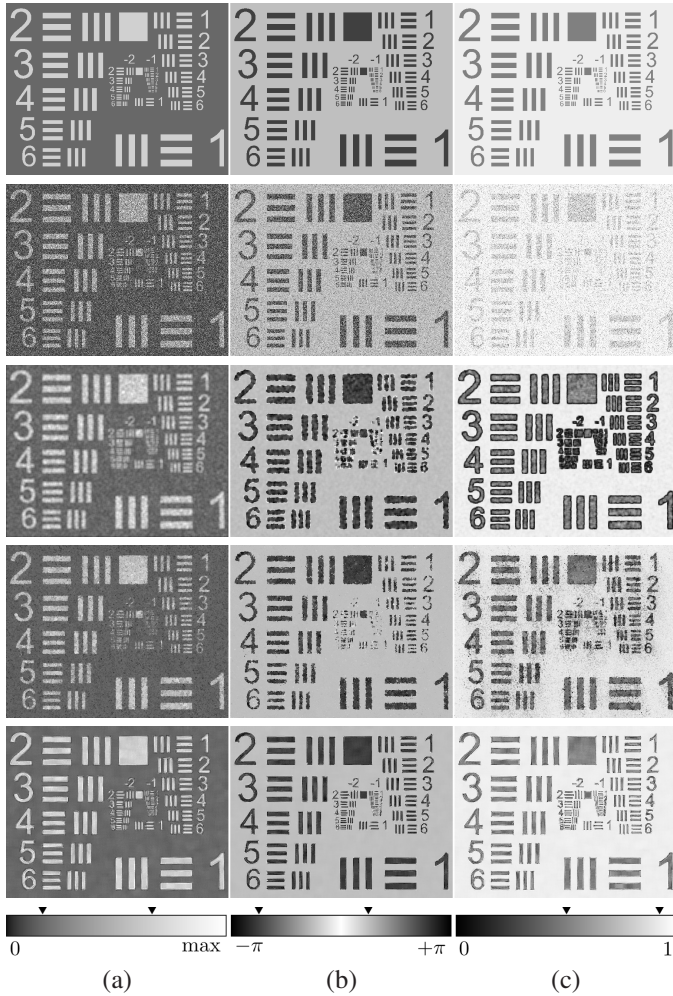
Fig. 6. (a) Reflectivity, (b) interferometric phase and (c) coherence of a resolution test pattern obtained from top to bottom by the ground truth, the SLC images (maximum likelihood estimator of [31]), the boxcar estimator, the IDAN estimator [26] and the NL-InSAR estimator. A colorbar of the range value is shown for each channel with pointers to indicate the underlying true values.

TABLE I
SNR VALUES OF ESTIMATED INSAR IMAGES USING DIFFERENT
ESTIMATORS AND THE COMPUTATION TIME

	Reflectivity	Phase	Coherence	Time (sec)
SLC Image [31]	-2.75	3.36	-1.19	–
WIN-SAR [15]	5.90	–	–	101.76
PEARLS [19]	–	5.27	–	394.83
Boxcar filter	6.47	5.90	-4.01	0.22
Lee [24]	6.23	9.12	2.03	0.77
IDAN [26]	5.00	7.88	0.33	522.53
NL-InSAR (non-it.)	6.26	8.70	5.82	148.39
NL-InSAR (10 it.)	**9.02**	**13.04**	**6.92**	1540.93

less spatial bias but has a higher variance. This is due in part to the edge-aligned windows containing less samples to reduce the variance, but also, to the window selection process which presents high variations. IDAN provides a good restoration of the edges but unfortunately a bias is introduced even in homogeneous area. This is due to the region growing method which tends to lower reflectivity and coherence values [26]. Moreover, the bias increases on the line since the adaptive neighborhood selects samples out of the line. As a result the variance is bigger than for the boxcar filter even if there are as many values to estimate the cross-correlation. We assume this phenomenon could be reduced by using a more suitable similarity criterion to define the region growing. NL-InSAR provides the best bias-variance trade-off. Indeed, comparatively to the boxcar filter, Lee's estimator and IDAN, (iterative) NL-InSAR is neither biased in homogeneous area nor around edges. Moreover, its variance is equivalent to the one of the boxcar filter in homogeneous area. NL-InSAR has a larger variance around edges than in homogeneous area since these regions present less redundant patterns. The non-iterative NL-InSAR provides a trade-off between the boxcar filter and the iterative NL-InSAR.

Figure 6 presents the obtained estimated images for two generated single-look complex images representing a 600×464 resolution test pattern. On the original resolution test pattern, the contrasts between the lowest value and highest value, for all channels, are the same as on the line cut of Figure 5. The images obtained with the NL-InSAR estimator seem to be well smoothed with a better edge and shape preservation. The images obtained by the boxcar and the IDAN estimators are more noisy than the images obtained by the NL-InSAR filter (the remaining variance is larger). Moreover, the boxcar estimator blurs the edges resulting in a loss of resolution and large underestimations of the coherence around edges. The IDAN filter preserves the shapes but the noise variance remains large essentially in the coherence image, and small details are lost essentially in the interferometric phase image. Finally, our NL-InSAR estimator seems to work efficiently by preserving small structures with a satisfying noise reduction.

To quantify the estimation qualities, Table I presents numerical results for the resolution test pattern shown on Figure 6. The performance criterion used is the signal to noise ratio (SNR):

$$SNR(\hat{u}, u) = 10 \log_{10} \frac{Var[u]}{\frac{1}{|\Omega|} \sum_{s \in \Omega} (u_s - \hat{u}_s)^2}. \quad (19)$$

filter to reach a satisfying estimation. Comparisons have been performed with the classical boxcar filter on a 7×7 sliding window, Lee's estimator [24], the IDAN filter with an adaptive neighborhood of maximum size 50 [26] and a non-iterative NL-InSAR with weights based only on the likelihood term with $h = 4$ (h is lower than in the iterative version to provide a more discriminant likelihood term to compensate the lack of the *prior* term).

Figure 5 shows the statistical answer of the five estimators on a cut through a line of width 10. The statistics have been measured on denoised images over 10 000 noisy generated images. The ground truth, the mean and an interval of variation (about 70% of the estimates) is represented on the graphics for the three estimated components. It can be noticed that the boxcar filter is unbiased with a low variance in homogeneous area but it presents a strong spatial bias around the edges of the rectangular function. This spatial bias produces large underestimations of the coherence around edges which is denoted in [24] as the dark ring effect. Lee's estimator presents

where u is a component of the ground truth image (e.g., the true reflectivity), $\hat{u}$ its estimate and Ω the image domain. Note that for the interferometric phase, we measure the SNR of the complex phase image $e^{j\hat{\beta}}$ to deal with phase wrapping as proposed in [19]. The results in term of SNR are compared again with the boxcar filter, Lee's estimator, IDAN, the non-iterative NL-InSAR and also with WIN-SAR [15] (a wavelet based amplitude filter) and PEARLS [19] (an adaptive local phase filter). NL-InSAR outperforms all the other filters for all components in term of SNR. In term of computation time, the boxcar filter and Lee's filter provide almost real-time denoising while the others require at least 100 sec to process a 600×464 image with an Intel Pentium D 32-bit, 3.20GHz. 10 iterations of NL-InSAR take three times as long as IDAN. If computation time is an issue, non-iterative NL-InSAR is three times faster than IDAN and still provides a better denoising in terms of SNR.

B. Results on True SLC SAR Data

This section presents an overview of results obtained on pairs of co-registered real single-look complex SAR images with the same InSAR estimators as above. The pairs of SAR images are assumed to follow Goodman's model presented in section I.

The first experiment is performed on images acquired simultaneously (mono-pass) over a single building of complex shape in Toulouse (France) by RAMSES (aerial sensor). They are in X band with a resolution under one meter in azimuth and slant range. Figure 7 presents the obtained estimates for the different denoising filters. The range is on the horizontal axis and the azimuth on the vertical axis. The algorithms are executed with the same parameters as described in Section IV-A. The results obtained with our NL-InSAR estimator seem to be well smoothed with a better edge and shape preservation than other filters. For instance, IDAN is unable to restore the edges of the building when these edges are not present in the amplitude images even though these edges are present in the interferometric phase image. This is also the case for the three trees on the left side of the image. Since NL-InSAR considers both the information of amplitude and phase, NL-InSAR restores the edges and the trees successfully. The speckle effect is strongly reduced and the spatial resolution seems to be well preserved: buildings, streets, and homogeneous areas are well restored in the three parameter images. Moreover, the bright scatterers (numerous in urban area) are well restored. Note that NL-InSAR preserves well the three bright lines on the left of the building whereas the boxcar filter blurs them and IDAN attenuates them. This attests the efficiency of the patch-based approach: the three lines acts as a rail on which the similarity patch slides in order to combine all pixels parallel to the bright lines. One can notice that very thin and dark structures are attenuated by NL-InSAR, such as the thin streets. This drawback might be avoided by using a smaller search window size to reduce the bias. In [19], [20], [37], [39]–[41], the authors propose to use adaptive search window size. Such approaches could possibly be used in NL-InSAR to reduce this undesired effect.

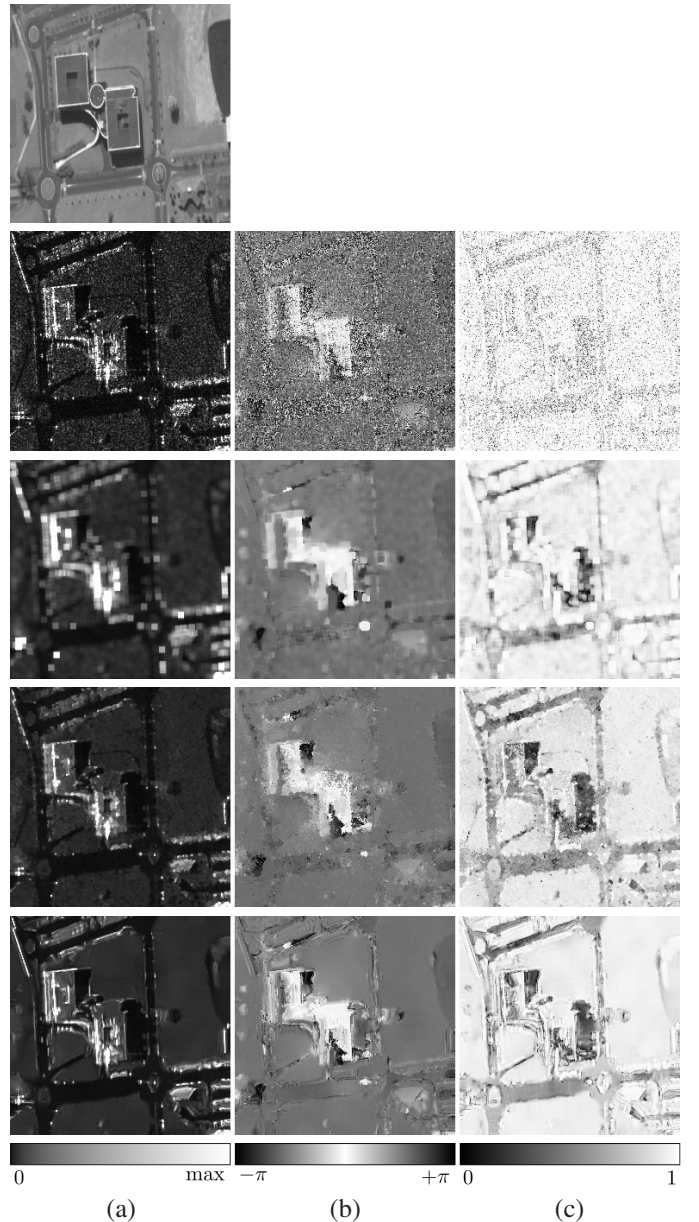| 0 | max | $-\pi$ | $+\pi$ | 0 | 1 |
| (a) | | (b) | | (c) | |

Fig. 7.   First line: orthophoto sensed by Quickbird ©DigitalGlobe. Following lines: (a) Reflectivity, (b) interferometric phase and (c) coherence of a building in Toulouse (France), RAMSES ©ONERA, obtained from top to bottom by the SLC images (maximum likelihood estimator of [31]), the boxcar estimator, the IDAN estimator [26] and the NL-InSAR estimator. A colorbar of the range value is shown for each channel.

The second experiment is performed on images acquired with a time difference of 22 days (dual-pass) over a wide area of Saint-Gervais-les-Bains (France) by TerraSAR-X (satellite sensor). They are in X band with a resolution of about three meters in azimuth and slant range. Figure 8 presents the obtained estimates for the different denoising filters. The range is on the horizontal axis and the azimuth on the vertical axis. Denoising this interferometric pair of images is challenging: resolution is low so most structures are only a few pixels wide, and coherence is poor in some regions due to temporal decorrelation and tropospheric variations. Given the limited redundancy of structures (very thin scale), the window sizes
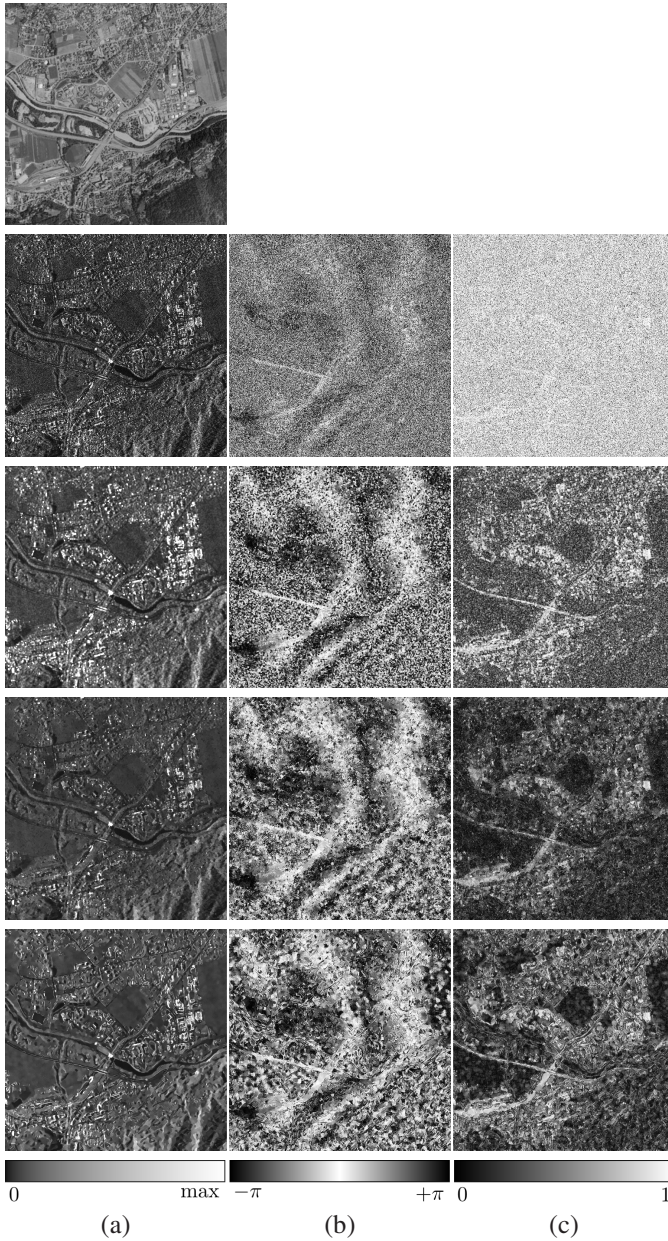
Fig. 8. First line: orthophoto sensed by the sensor of the Institut Géographique National (IGN) ©GEOPORTAIL 2007. Following lines: (a) Reflectivity, (b) interferometric phase and (c) coherence of Saint-Gervais-les-Bains (France), TerraSAR-X ©DLR, obtained from top to bottom by the SLC images (maximum likelihood estimator of [31]), the boxcar estimator, the IDAN estimator [26] and the NL-InSAR estimator. A colorbar of the range value is shown for each channel.

have been reduced to better preserve the details (search window $|W|$ set to 9×9, patch size $|\Delta|$ set to 3×3, and h and T parameters set to $h = 5.3$ and $T = 0.2|\Delta|$ as recommended in [17]). We still use $L_{min} = 10$ and 10 iterations. The classical boxcar filter is performed with a 3×3 window and the IDAN filter with an adaptive neighborhood of maximum size 10. NL-InSAR clearly improves on the boxcar filter, even with low coherence and low resolution data. The edges seem better preserved than with IDAN filter and the remaining noise variance in the interferometric phase is lower.

V. CONCLUSION

A new method was proposed for SAR interferogram estimation. This method is based on the non-local means filter [27] whose originality rests on the weighted combination of pixel values which can be far apart. We apply the general iterative methodology proposed in [17] to select suitable pixels by evaluating a patch-based similarity considering noisy amplitudes, noisy interferometric phases and previous estimates. Finally, the reflectivity, the actual interferometric phase and the coherence are jointly estimated. The proposed estimator out-performs state-of-the-art estimators in terms of both noise reduction and edge preservation. The noise, present in the input images, is well smoothed in the homogeneous regions and the object contours are well restored (preservation of the resolution). Moreover we can consider from our experiments that the reflectivity, the actual interferometric phase and the coherence are well recovered, without introducing strong undesired artifacts and with a good restoration of bright scatterers. Even if the performance of non-local approaches is best when the scale of the structures in the image is larger than the resolution, our method provides results comparable or better to the state-of-the-art on data with low and high resolutions. A drawback of this estimator is the attenuation of thin and dark details in the regularized images. In a future work, we will try to better preserve these structures by using adaptive patch-size selection. The filter elaboration, based on the statistics of the processed images, has led to define a suitable patch-similarity criterion for InSAR images. This similarity criterion could be applied in the future to other applications such as pattern tracking and displacement estimation.

APPENDIX A
SIMILARITY LIKELIHOOD

The similarity likelihood is given by the triple integral

$$\mathcal{I}_3 = \iiint p(A_1, A_1', \phi_1 | R, D, \beta) p(A_2, A_2', \phi_2 | R, D, \beta) dR \, dD \, d\beta.$$

Starting the integration calculus on the variable β, the following simple integral has to be solved:

$$\mathcal{I}_1 = \int \exp\left[\lambda\left(A_1 A_1' \cos(\phi_1 - \beta) + A_2 A_2' \cos(\phi_2 - \beta)\right)\right] d\beta$$

with $\lambda = \frac{2D}{R(1-D^2)}$. Integrating by substitution $\psi \leftarrow \beta + \phi_2$ and developing the cosine functions gives:

$$\mathcal{I}_1 = \int \exp\left[\lambda\left(A_2 A_2' + A_1 A_1' \cos(\Delta\phi)\right) \cos(\psi) + \right.$$
$$\left. \lambda\left(A_1 A_1' \sin(\Delta\phi)\right) \sin(\psi)\right] d\psi$$

with $\Delta\phi = \phi_1 - \phi_2$. Then, by using eq. 3.937.2 in [42]:

$$\mathcal{I}_1 = 2\pi J_0\left(j \frac{2D\sqrt{A_1^2 A_1'^2 + A_2^2 A_2'^2 + 2A_1 A_1' A_2 A_2' \cos\Delta\phi}}{R(1-D^2)}\right)$$

with J_n the Bessel function of the first kind. Pursuing on the variable R gives the following integral:

$$\mathcal{I}_2 = \int \frac{1}{R^4} \exp\left(-\frac{A_1^2 + A_1'^2 + A_2^2 + A_2'^2}{R(1-D^2)}\right) \mathcal{I}_1 dR.$$

Using the integration by substitution $x \leftarrow 1/R(1-D^2)$ gives:

$$\mathcal{I}_2 = 2\pi(1-D^2)^3 \int x^2 \exp\left(-x(A_1^2 + A_1'^2 + A_2^2 + A_2'^2)\right)$$
$$J_0\left(jx2D\sqrt{A_1^2 A_1'^2 + A_2^2 A_2'^2 + 2A_1 A_1' A_2 A_2' \cos\Delta\phi}\right) dx.$$

According to eq. 6.621.4 in [42]:

$$\mathcal{I}_2 = 2\pi(1-D^2)^3 \left(\frac{2\mathcal{A} + D^2\mathcal{B}}{\sqrt{\mathcal{A} - D^2\mathcal{B}}^5}\right)$$

with $\quad \mathcal{A} = (A_1^2 + A_1'^2 + A_2^2 + A_2'^2)^2$

and $\quad \mathcal{B} = 4(A_1^2 A_1'^2 + A_2^2 A_2'^2 + 2A_1 A_1' A_2 A_2' \cos\Delta\phi).$

Finally, the triple integral can be expressed by the following single integral on the variable D:

$$\mathcal{I}_3 = \frac{8}{\pi}\mathcal{C} \int \frac{(1-D^2)(2\mathcal{A} + D^2\mathcal{B})}{\sqrt{\mathcal{A} - D^2\mathcal{B}}^5} dD.$$
$$\text{with } \mathcal{C} = A_1 A_1' A_2 A_2'$$

Developing the expression and using integration by substitution $x \leftarrow D^2$, the following holds:

$$\mathcal{I}_3 = \frac{8}{\pi}\mathcal{C} \left[\frac{1}{\sqrt{\mathcal{A}}^3} \int \frac{x^{-1/2}}{\sqrt{1-x\mathcal{B}/\mathcal{A}}^5} dx + \right.$$
$$\frac{\mathcal{B} - 2\mathcal{A}}{2\sqrt{\mathcal{A}}^5} \int \frac{x^{1/2}}{\sqrt{1-x\mathcal{B}/\mathcal{A}}^5} dx -$$
$$\left.\frac{\mathcal{B}}{2\sqrt{\mathcal{A}}^5} \int \frac{x^{3/2}}{\sqrt{1-x\mathcal{B}/\mathcal{A}}^5} dx\right].$$

According to eq 3.194.1 in [42]:

$$\mathcal{I}_3 = \frac{8}{\pi}\mathcal{C} \left[\frac{1}{\sqrt{\mathcal{A}}^3} \left(2\,_2F_1(\frac{5}{2}, \frac{1}{2}; \frac{3}{2}; \frac{\mathcal{B}}{\mathcal{A}})\right) + \right.$$
$$\frac{\mathcal{B} - 2\mathcal{A}}{2\sqrt{\mathcal{A}}^5} \left(\frac{2}{3}\,_2F_1(\frac{5}{2}, \frac{3}{2}; \frac{5}{2}; \frac{\mathcal{B}}{\mathcal{A}})\right) -$$
$$\left.\frac{\mathcal{B}}{2\sqrt{\mathcal{A}}^5} \left(\frac{2}{5}\,_2F_1(\frac{5}{2}, \frac{5}{2}; \frac{7}{2}; \frac{\mathcal{B}}{\mathcal{A}})\right)\right]$$

with $_2F_1$ an hyper-geometric function. Finally, by developing the hyper-geometric function, the triple integral is equal to:

$$\mathcal{I}_3 = \frac{8\mathcal{C}}{\pi\sqrt{\mathcal{B}}^3} \left(\frac{\mathcal{A} + \mathcal{B}}{\mathcal{A}}\sqrt{\frac{\mathcal{B}}{\mathcal{A} - \mathcal{B}}} - \arcsin\sqrt{\frac{\mathcal{B}}{\mathcal{A}}}\right).$$

APPENDIX B
SIMILARITY ON THE ESTIMATES

The similarity on the estimate is defined from the Kullback Leibler divergence between two data distributions $p(A, A', \Delta\phi|R_1, D_1, \beta_1)$ and $p(A, A', \Delta\phi|R_2, D_2, \beta_2)$. It is equivalent to considering the Kullback Leibler divergence between $p(z|\Sigma_1)$ and $p(z|\Sigma_2)$ with Σ_k as defined in (2) and $R_k = R_k'$, $k = 1..2$. The Kullback Leibler divergence between two zero-mean complex circular Gaussian distributions is given by:

$$D_{KL}(\Sigma_1|\Sigma_2) = \frac{2}{\pi}\left[\log\left(\frac{\det\Sigma_1}{\det\Sigma_2}\right) + tr\left(\Sigma_1^{-1}\Sigma_2\right) - 2\right].$$

The symmetrical version of the Kullback Leibler divergence is then:

$$SD_{KL}(\Sigma_1|\Sigma_2) = D_{KL}(\Sigma_1|\Sigma_2) + D_{KL}(\Sigma_2|\Sigma_1)$$
$$= \frac{2}{\pi}\left[tr\left(\Sigma_1^{-1}\Sigma_2\right) + tr\left(\Sigma_2^{-1}\Sigma_1\right) - 4\right].$$

Note that with $R_k = R_k'$, $k = 1..2$:

$$tr(\Sigma_1^{-1}\Sigma_2) = 2\left[\frac{R_2(1 - D_1 D_2 \cos(\beta_1 - \beta_2))}{R_1(1 - D_1^2)}\right],$$
$$tr(\Sigma_2^{-1}\Sigma_1) = 2\left[\frac{R_1(1 - D_2 D_1 \cos(\beta_1 - \beta_2))}{R_2(1 - D_2^2)}\right].$$

Then the symmetrical Kullback Leibler divergence is given by:

$$SD_{KL}(\Sigma_1, \Sigma_2) = \frac{4}{\pi}\left[\frac{R_1}{R_2}\left(\frac{1 - D_1 D_2 \cos(\beta_1 - \beta_2)}{1 - D_2^2}\right) + \frac{R_2}{R_1}\left(\frac{1 - D_1 D_2 \cos(\beta_1 - \beta_2)}{1 - D_1^2}\right) - 2\right]$$

REFERENCES

[1] N. Bechor and H. Zebker, "Measuring two-dimensional movements using a single InSAR pair," *Geophysical Research Letters*, vol. 33, p. 16, 2006.
[2] R. Hanssen, *Radar interferometry*. Kluwer Academic, 2001.
[3] N. Goodman, "Statistical analysis based on a certain multivariate complex Gaussian distribution (an introduction)," *Annals of Mathematical Statistics*, pp. 152–177, 1963.
[4] R. Bamler and P. Hartl, "Synthetic aperture radar interferometry," *Inverse problems*, vol. 14, pp. R1–R54, 1998.
[5] J.-S. Lee, "Speckle analysis and smoothing of synthetic aperture radar images," *Computer Graphics and Image Processing*, vol. 17, no. 1, pp. 24–32, September 1981.
[6] D. Kuan, A. Sawchuk, T. Strand, and P. Chavel, "Adaptive noise smoothing filter for images with signal-dependent noise," *IEEE Transactions on Pattern Analysis and Machine Intelligence*, vol. 7, no. 2, pp. 165–177, 1985.
[7] Y. Wu and H. Maître, "Smoothing speckled synthetic aperture radar images by using maximum homgeneous region filters," *Optical Engineering*, vol. 31, p. 1785, 1992.
[8] A. Lopes, E. Nezry, R. Touzi, and H. Laur, "Maximum a posteriori speckle filtering and first order texture models in SAR images," in *Geoscience and Remote Sensing Symposium, 1990. IGARSS'90.*, 1990, pp. 2409–2412.
[9] V. Frost, J. Stiles, K. Shanmugan, and J. Holtzman, "A model for radar images and its application to adaptive digital filtering of multiplicative noise," *IEEE Transactions on Pattern Analysis and Machine Intelligence*, vol. 4, pp. 157–166, 1982.
[10] R. Touzi, "A review of speckle filtering in the context of estimation theory," *IEEE Transactions on Geoscience and Remote Sensing*, vol. 40, no. 11, pp. 2392–2404, 2002.
[11] F. Argenti and L. Alparone, "Speckle removal from SAR images in the undecimated wavelet domain," *IEEE Transactions on Geoscience and Remote Sensing*, vol. 40, no. 11, pp. 2363–2374, 2002.

[12] T. Bianchi, F. Argenti, and L. Alparone, "Segmentation-Based MAP Despeckling of SAR Images in the Undecimated Wavelet Domain," *IEEE Transactions on Geoscience and Remote Sensing*, vol. 46, no. 9, pp. 2728–2742, 2008.

[13] M. Bhuiyan, M. Ahmad, and M. Swamy, "Spatially adaptive wavelet-based method using the Cauchy prior for denoising the SAR images," *IEEE Transactions on Circuits and Systems for Video Technology*, vol. 17, no. 4, pp. 500–507, 2007.

[14] H. Xie, L. Pierce, and F. Ulaby, "SAR speckle reduction using wavelet denoising and Markov random field modeling," *IEEE Transactions on Geoscience and Remote Sensing*, vol. 40, no. 10, pp. 2196–2212, 2002.

[15] A. Achim, P. Tsakalides, and A. Bezerianos, "SAR image denoising via Bayesian wavelet shrinkage based on heavy-tailed modeling," *IEEE Transactions on Geoscience and Remote Sensing*, vol. 41, no. 8, pp. 1773–1784, 2003.

[16] X. Yang and D. Clausi, "Structure-preserving Speckle Reduction of SAR Images using Nonlocal Means Filters," in *IEEE International Conference on Image Processing*, 2009.

[17] C. Deledalle, L. Denis, and F. Tupin, "Iterative Weighted Maximum Likelihood Denoising with Probabilistic Patch-Based Weights," *IEEE Transactions on Image Processing*, vol. 18, no. 12, pp. 2661–2672, 2009.

[18] E. Trouvé, M. Caramma, and H. Maître, "Fringe detection in noisy complex interferograms," *Applied Optics*, vol. 35, no. 20, pp. 3799–3806, 1996.

[19] J. Bioucas-Dias, V. Katkovnik, J. Astola, and K. Egiazarian, "Absolute phase estimation: adaptive local denoising and global unwrapping," *Applied Optics*, vol. 47, no. 29, pp. 5358–5369, 2008.

[20] V. Katkovnik, J. Astola, and K. Egiazarian, "Phase local approximation (PhaseLa) technique for phase unwrap from noisy data," *IEEE Transactions on Image Processing*, vol. 17, no. 6, pp. 833–846, 2008.

[21] R. Touzi, A. Lopes, J. Bruniquel, and P. Vachon, "Coherence estimation for SAR imagery," *IEEE Transactions on Geoscience and Remote Sensing*, vol. 37, no. 1 Part 1, pp. 135–149, 1999.

[22] C. Gierull, D. Establ, and O. Ottawa, "Unbiased coherence estimator for SAR interferometry with application to moving target detection," *Electronics Letters*, vol. 37, no. 14, pp. 913–915, 2001.

[23] C. López Martínez, X. Fàbregas Cànovas, and E. Pottier, "Wavelet Transform-Based Interferometric SAR Coherence Estimator," *IEEE Signal processing letters*, vol. 12, no. 12, pp. 831–834, 2005.

[24] J. Lee, S. Cloude, K. Papathanassiou, M. Grunes, and I. Woodhouse, "Speckle filtering and coherence estimation of polarimetric SAR interferometry data for forest applications," *IEEE Transactions on Geoscience and Remote Sensing*, vol. 41, no. 10 Part 1, pp. 2254–2263, 2003.

[25] J. Lee, M. Grunes, and G. De Grandi, "Polarimetric SAR speckle filtering and its implication for classification," *IEEE Transactions on Geoscience and Remote Sensing*, vol. 37, no. 5 Part 2, pp. 2363–2373, 1999.

[26] G. Vasile, E. Trouvé, J. Lee, and V. Buzuloiu, "Intensity-Driven Adaptive-Neighborhood Technique for Polarimetric and Interferometric SAR Parameters Estimation," *IEEE Transactions on Geoscience and Remote Sensing*, vol. 44, no. 6, pp. 1609–1621, 2006.

[27] A. Buades, B. Coll, and J. Morel, "A Non-Local Algorithm for Image Denoising," *Computer Vision and Pattern Recognition, 2005. CVPR 2005. IEEE Computer Society Conference on*, vol. 2, 2005.

[28] J. Goodman, *Speckle phenomena in optics: theory and applications*. Roberts & Company Publishers, 2006.

[29] J. Fan, M. Farmen, and I. Gijbels, "Local maximum likelihood estimation and inference," *Journal of the Royal Statistical Society. Series B, Statistical Methodology*, pp. 591–608, 1998.

[30] J. Polzehl and V. Spokoiny, "Propagation-separation approach for local likelihood estimation," *Probability Theory and Related Fields*, vol. 135, no. 3, pp. 335–362, 2006.

[31] M. Seymour and I. Cumming, "Maximum likelihood estimation for SAR interferometry," in *The 1994 International Geoscience and Remote Sensing Symposium.*, vol. 4, 1994, pp. 2272–2274.

[32] J. Lee, "Digital image smoothing and the sigma filter," *Computer Vision, Graphics, and Image Processing*, vol. 24, pp. 255–269, 1983.

[33] L. Yaroslavsky, *Digital Picture Processing*. Springer-Verlag New York, Inc. Secaucus, NJ, USA, 1985.

[34] C. Tomasi and R. Manduchi, "Bilateral filtering for gray and color images," in *Computer Vision, 1998. Sixth International Conference on*, 1998, pp. 839–846.

[35] A. Buades, B. Coll, and J. Morel, "A Review of Image Denoising Algorithms, with a New One," *Multiscale Modeling and Simulation*, vol. 4, no. 2, p. 490, 2005.

[36] P. Coupe, P. Yger, and C. Barillot, "Fast Non Local Means Denoising for 3D MR Images," *Lecture Notes In Computer Science*, vol. 4191, pp. 33–40, 2006.

[37] B. Goossens, H. Luong, A. Pižurica, and W. Philips, "An improved non-local denoising algorithm," in *Proc. Int. Workshop on Local and Non-Local Approximation in Image Processing (LNLA'2008), Lausanne, Switzerland*, 2008.

[38] J. Darbon, A. Cunha, T. Chan, S. Osher, and G. Jensen, "Fast nonlocal filtering applied to electron cryomicroscopy," *Biomedical Imaging: From Nano to Macro, 2008. ISBI 2008. 5th IEEE International Symposium on*, pp. 1331–1334, 2008.

[39] G. Gilboa, N. Sochen, and Y. Zeevi, "Estimation of optimal PDE-based denoising in the SNR sense," *IEEE Transactions on Image Processing*, vol. 15, no. 8, pp. 2269–2280, 2006.

[40] C. Kervrann and J. Boulanger, "Local Adaptivity to Variable Smoothness for Exemplar-Based Image Regularization and Representation," *International Journal of Computer Vision*, vol. 79, no. 1, pp. 45–69, 2008.

[41] N. Azzabou, N. Paragios, and F. Guichard, "Uniform and textured regions separation in natural images towards MPM adaptive denoising," *Lecture Notes in Computer Science*, vol. 4485, p. 418, 2007.

[42] I. Gradshteyn, I. Ryzhik, and A. Jeffrey, *Table of integrals, series, and products*. Academic Press, 1980.

Charles-Alban Deledalle (S'08) received the engineering degree from Ecole Pour l'Informatique et les Techniques Avancées (EPITA) and the Science & Technology master's degree from the University Pierre et Marie Curie (Paris 6), both in Paris in 2008. He is currently pursuing the Ph.D. degree at Telecom ParisTech. His main interests are image denoising, analysis and interpretation, especially in multi-modal synthetic aperture radar imagery.

Loïc Denis received the Engineer degree from Ecole Superieure de Chimie Physique Électronique de Lyon (CPE Lyon), France, in 2003 and the Ph.D. degree from St-Étienne University, France, in 2006. In 2006–2007, he was a Postdoctor with Telecom ParisTech, France, where he worked on 3-D reconstruction from interferometric SAR and optical data. From 2007 to the beginning of 2010, he was Assistant Professor with CPE Lyon, France. He joined the Observatory of Lyon in 2010 to work on image reconstruction in astronomy and biomedical imaging. His research interests include image denoising and reconstruction, radar image processing, deconvolution and digital holography.

Florence Tupin (SM'07) received the engineering degree from Ecole Nationale Supérieure des Télécommunications (ENST) of Paris in 1994, and the Ph.D. degree from ENST in 1997. She is currently Professor at Telecom ParisTech in the TSI (Image and Signal Processing) Department. Her main research interests are image analysis and interpretation, 3D reconstruction, Markov random field techniques, and synthetic aperture radar, especially for urban remote sensing applications.